Journal of Applied Physics

RESEARCH ARTICLE | JUNE 30 2023

Uncertainty evaluation of Monte Carlo simulated line scan profiles of a critical dimension scanning electron microscope (CD-SEM)

M. S. S. Khan ; S. F. Mao ; Y. B. Zou ; Y. G. Li ; B. Da ; Z. J. Ding

J. Appl. Phys. 133, 245303 (2023)
https://doi.org/10.1063/5.0153379

Journal of Applied Physics ARTICLE pubs.aip.org/aip/jap

Uncertainty evaluation of Monte Carlo simulated line scan profiles of a critical dimension scanning electron microscope (CD-SEM)

Cite as: J. Appl. Phys. **133**, 245303 (2023); doi: 10.1063/5.0153379
Submitted: 7 April 2023 · Accepted: 7 June 2023 ·
Published Online: 30 June 2023

M. S. S. Khan,[1,2] S. F. Mao,[3] Y. B. Zou,[4] Y. G. Li,[2,a)] B. Da,[5] and Z. J. Ding[1,6,a)]

AFFILIATIONS

[1]Department of Physics, University of Science and Technology of China, Hefei, Anhui 230026, People's Republic of China
[2]Key Laboratory of Materials Physics, Institute of Solid State Physics, Chinese Academy of Sciences, Hefei, Anhui 230031, People's Republic of China
[3]Department of Nuclear Science and Engineering, University of Science and Technology of China, Hefei, Anhui 230026, People's Republic of China
[4]School of Physics and Electronic Engineering, Xinjiang Normal University, Urumchi, Xinjiang 830054, People's Republic of China
[5]Center for Basic Research on Materials, National Institute for Materials Science, Tsukuba, Ibaraki 305-0044, Japan
[6]Hefei National Research Center for Physical Sciences at the Microscale, University of Science and Technology of China, Hefei, Anhui 230026, People's Republic of China

[a)]**Authors to whom correspondence should be addressed:** ygli@theory.issp.ac.cn and zjding@ustc.edu.cn

ABSTRACT

In recent years, precision and accuracy for a more precise critical dimension (CD) control have been required in CD measurement technology. CD distortion between the measurement by a critical dimension scanning electron microscope (CD-SEM) and a reference tool is the most important factor for a more accurate CD measurement. CD bias varies by a CD-SEM and a pattern condition. Therefore, it is urgently needed to identify, characterize, and quantify those parameters that may or may not affect the CD measurement by a CD-SEM. The sensitivity of the Monte Carlo simulated CD-SEM images with multiple physical modeling components has been studied previously. In this study, we demonstrate that the work function and elastic scattering potential models have a significant impact on secondary electron emission intensity, but their influence on the shape of the linescan profile is small, and other factors like the optical energy loss function and dielectric function models have even smaller effects. We have evaluated the uncertainty in the linescan profiles of Si line structures with different sidewall angles due to several different physical factors. It is found that when the CD is evaluated by a peak/valley method, the uncertainty of the CD is negligible. Therefore, it is concluded that the CD value and its related uncertainty are not critically related to the physical factors of the present Monte Carlo simulation model but rely dominantly on the line structure and electron beam parameters.

I. INTRODUCTION

Monte Carlo simulation techniques in microbeam analysis, electron beam lithography, electron spectroscopy, and scanning electron microscopy (SEM) have been in use for decades.[1–10] The demand for Monte Carlo simulation study of scanning electron microscope (SEM) imaging[11] mainly comes from the interpretation of the image contrast and imaging mechanisms in experiments. In recent years, the application of the Monte Carlo technique to critical dimension scanning electron microscope (CD-SEM) images has become an important topic for industrial application.[12]

In the semiconductor industry, the CD-SEM is a specialized length measuring instrument for the critical dimension (CD) measurement of nanostructures[13] in the integrated circuit due to its high resolution, fast imaging speed, and non-destructive processing. The CD is the minimum geometrical feature size in the wafer

limited by photolithography technology used for the fabrication process; it is one of the important quantities in dimensional metrology. Accurate CD measurements are needed to meet the strict dimensional control requirements in manufacturing. The accuracy of the measured CD values is a challenging issue with very tight specifications in process control for mask and wafer fabrication. Secondary electron imaging is the mode used in CD-SEM observation, which allows one to observe the sample structure with high contrast. CD metrology based on secondary electron imaging consists of two steps, namely, pixel-based secondary electron signal imaging and subsequent extraction of CD values from the intensity profile of secondary electron signals for edge detection by an appropriate algorithm.[14] A secondary electron image is a point-by-point representation of the secondary electron intensity produced by a raster scan of the primary electron beam across the sample surface. The secondary electron intensity at a given position on the sample surface is contributed by the secondary electrons emitted from the nearby locations around the incident position in the excited volume. In a secondary electron image of a line structure, the line edges are usually brighter than their surroundings due to the edge effect resulting from the enhanced effective emission area around the edge than elsewhere. Therefore, the secondary electron profile has a characteristic peak with a certain extension at an edge.[15]

CD metrology relies on the understanding of the relationship between the intensity profile of secondary electron signals and the sample structure. Although the CD-SEM has a good contrast and high resolution, it is still subjected to an unavoidable error in CD metrology because the intensity of secondary electron signals is a complicated function of the instrument setup, specimen geometric structure, and material composition. An empirical method for CD metrology is based on the artificially specified brightness threshold or, in some special cases, is determined by using a reference sample.[16] The methods described for CD measurement include a line-fit algorithm,[13] linear regression to baseline, maximal derivative, sigmoidal fit,[17] and profile characterization of several parameters.[18,19] These empirical algorithms have limitations, e.g., arbitrary CD definitions[13] and single-valued CD; they might be useful only under certain conditions but give incorrect estimates under other conditions. Furthermore, dimensional metrology based on secondary electron imaging has greater potential in 3D metrology, and the empirical algorithm cannot meet the needs in this area.

The CD metrology would include significant uncertainty if it were not having a solid physical background of a secondary electron signal generation mechanism. A physical modeling based metrology algorithm should be the best way to meet the measurement tolerances and strict CD control requirements. Thus, the Monte Carlo simulation technique by modeling electron interaction processes in the sample has played an important role in developing the CD metrology algorithm[20–24] to derive an accurate method for linewidth determination. Several simple algorithms have been proposed for determining linewidths based on the Monte Carlo simulation results in different areas.[25–31] These CD determination methods are approximate and also have certain limitations for the application circumstances. To overcome the limitations, a model-based library (MBL) method was proposed[28–36] and adopted by an ISO standard.[37] By this MBL method, a Monte Carlo simulation method that models the physical process of electron beam interaction with a specimen in the CD-SEM imaging is used to establish a numerical data library of simulated linescan profiles for various concerned experimental parameters. The Monte Carlo simulation makes it possible to establish a one-to-one relationship between the secondary electron linescan profile, the geometric structure, and the beam condition. The MBL method could be an ideal tool for CD-SEM metrology at advanced nodes for its high accuracy, and its effectiveness has been verified experimentally.[34,35]

Despite extensive theoretical and experimental works done aiming for accurate estimation of the CD, however, the evaluation of the error sources and uncertainty has been rarely reported so far. The uncertainty in CD may depend on several experimental factors, including electron beam conditions (e.g., angle of incidence, beam diameter, and focusing), sample structure (structural shape and related parameters, e.g., top and bottom line widths, line height, sidewall angles, top rounding, and footing for a trapezoidal line structure). Particularly, the uncertainty in CD determination due to the physical factors (work function, energy loss function, and elastic and inelastic mean free path calculation models) in a Monte Carlo modeling employed by the MBL method has also not been fully investigated. Only sensitivity analysis of the effects of, for example, inelastic scattering cross section, model sensitivity, sidewall roughness, and surface potential on the linewidth measurements has been performed.[38–41] In this study, we have performed a CD-SEM image simulation combined with some of the uncertainties to arrive at a more detailed characterization of CD-SEM measurements of the CD. It should be noted that certain uncertainties associated with systematic errors, unknown beam size, and unknown edge angle are not explicitly addressed in this study because the focus of our analysis lies on evaluating and quantifying theoretical uncertainties within the context of the simulated CD-SEM images.

First, all error sources of uncertainties considered here in the Monte Carlo modeling of CD-SEM imaging are sorted into two categories: (1) the input of material properties (i.e., work function and optical constants of the material) and (2) modeling of electron scattering cross sections (i.e., scattering potential for the calculation of electron elastic scattering cross section and dielectric function model for the calculation of electron inelastic scattering cross section). The measurement uncertainty is then evaluated according to the principle of a Monte Carlo uncertainty quantification approach,[42,43] whose standard procedure consists of the following steps: (a) definition of the measurand and inputs, (b) modeling, (c) estimation of probability density functions for the inputs, (d) setup and execution of the Monte Carlo simulations, and (e) summary and presentation of the results. In the following, the chief elements in this uncertainty quantification process are described.

II. THEORETICAL MODEL

We have adopted our up-to-date simulation code, Classical Trajectory Monte Carlo simulation of Scanning Electron Microscopy (CTMC-SEM),[44,45] for this calculation. The simulation of the generation and emission processes of secondary electron signals is performed by tracing incident electron trajectories inside

the bulk of a sample with a random sampling technique for electron elastic and inelastic scattering events.

A. Geometric representation

The 3D sample structure modeling and the optimization for a fast simulation are the two main aspects of a Monte Carlo simulation of the CD-SEM image of a complex geometric structure. Most of the samples in actual observations have various complicated surface morphologies or 3D structures. In this study, for the purpose of uncertainty quantification of the CD, we have considered only the simple trapezoidal-like structure. This is because we aim to evaluate the uncertainty of simulation while ignoring the uncertainties due to geometric structure parameters. Here, a line structure with a rectangle-shaped cross section is considered, and all the surfaces are smooth by ignoring the surface roughness. A 3D structure can be constructed by several approaches, e.g., a simple constructive solid geometry approach has been employed for SEM imaging.[46,47] The geometric structure used in this study is based on our previous work by using a finite element triangular mesh.[48–51] The triangular mesh of a line structure is constructed with the aid of Gmsh, a freely available GNU (General Public License) meshing software.[52] Figure 1 shows a constructed silicon line structure, made of three lines in a 50×50 nm rectangle-shaped cross section corresponding to a 90° sidewall angle and placed on a silicon substrate (the density of 2.329 g/cm^3). We have also employed the space subdivision method to accelerate our Monte Carlo simulation. This technique involves dividing the simulated material volume into smaller regions or cells with a 3D finite element mesh of the sample surface to improve the computational efficiency of electron trajectory simulation in the 3D target. Please refer to Ref. 48 for further details on the space subdivision method used in our study.

B. Elastic scattering model

The sensitivity of the simulated secondary electron signals to the elastic scattering cross section models has been less investigated in the literature. Elastic scattering happens when an electron is deflected by the nuclear potential of an atom without a change of kinetic energy. The exact probability of the scattering events and the probability distribution of the deflected angles are described by Mott's cross sections,[53] whose formulation was derived from the solution of the Dirac equation for a kinetic electron moving in an atomic potential

$$\frac{d\sigma_e}{d\Omega} = |f(\theta)|^2 + |g(\theta)|^2, \tag{1}$$

where σ_e is the elastic cross section, $f(\theta)$ and $g(\theta)$ are the scattering amplitudes that can be calculated with the partial wave expansion method

$$f(\theta) = \frac{1}{2iK}\sum_{l=0}^{\infty}\left\{(\ell+1)\left(e^{2i\delta_\ell^+}-1\right)+\ell\left(e^{2i\delta_\ell^-}-1\right)\right\}P_\ell(\cos\theta), \tag{2}$$

$$g(\theta) = \frac{1}{2iK}\sum_{\ell=1}^{\infty}\left\{-e^{2i\delta_\ell^+}+e^{2i\delta_\ell^-}\right\}P_\ell^1(\cos\theta), \tag{3}$$

where $\hbar K$ is the momentum of the electron; δ_l^+ and δ_l^- are spin up and spin down phase shifts of the ℓth partial wave, respectively; $P_\ell(\cos\theta)$ and $P_\ell^1(\cos\theta)$ are the Legendre and the first order associated Legendre functions, respectively.

The phase shifts are calculated from a radial equation of the electron motion in a potential field $V(r)$, where r represents the distance from the atomic nucleus of a target atom placed at the origin of the coordinate system. The effective interaction potential for a projectile electron at a given distance r can be described by means of an optical potential model

$$V(r) = V_{st}(r) + V_{ex}(r) + V_{cp}(r) - iW_{abs}(r), \tag{4}$$

where $V_{st}(r)$ is the electrostatic potential, $V_{ex}(r)$ is the exchange potential, $V_{cp}(r)$ is the correlation-polarization potential, and $W_{abs}(r)$ is the absorption potential (W_{abs} is taken zero in this study). There are various potential models, which may significantly affect the calculated Mott's cross section and, hence, the scattering potential model plays the role of an uncertainty factor in a Monte Carlo simulation.

We have used Salvat's latest version of Fortran 90 code, Elastic Scattering of Electrons and Positrons by Atoms (ELSEPA),[54] to calculate Mott's cross sections for 384 different scattering potential models in the whole interested electron kinetic energy region from primary energy down to the potential barrier for the secondary

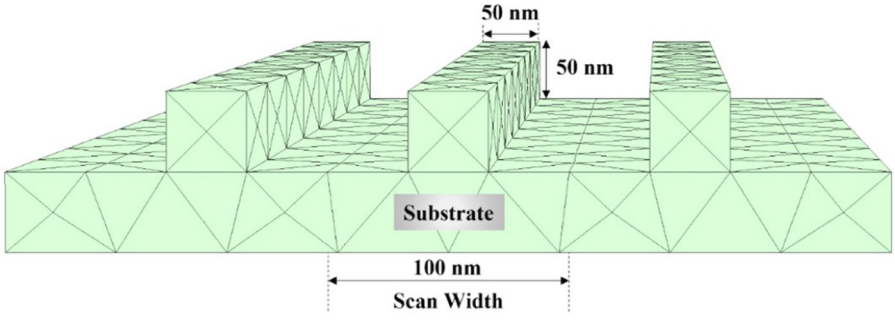

FIG. 1. 3D finite element triangular mesh of the line structure.

electron emission. In all these Mott's cross sections, we have considered four nuclear charge distribution models, four electron distribution models, four electron exchange potential models, and three correlation-polarization potential models. For each of these potential models, we have considered both free atomic potential and the muffin-tin potential, resulting in a total of 384 (=4 × 4 × 4 × 3 × 2) different scattering potentials.[55] In the following examples, "No. 42001" elastic cross section is used where "4" stands for Helm's nuclear charge distribution model, "2" for the Thomas–Fermi–Dirac electron distribution model, "0" for the non-exchange potential, "0" for the non-correlation-polarization potential, and "1" for the muffin-tin atomic potential model.

C. Inelastic scattering models

Unlike elastic scattering events, an electron changes both kinetic energy and momentum in an inelastic scattering event. These events play a critical role in secondary electron generation. Energy loss processes include electron interactions with valence electrons (single particle and plasmon excitations), inner-shell electrons (interband transitions and ionizations), and the solid lattice (longitudinal optical phonon excitations). These energy loss mechanisms are described by the optical constants or the energy loss function according to the dielectric functional theory, and these energy loss channels for a kinetic electron are simulated discretely with the use of the energy loss function. The differential inelastic scattering cross section for an electron moving in a solid of the dielectric function, $\varepsilon(q, \omega)$, is expressed in terms of the differential inverse inelastic mean free path[56]

$$\frac{d^2\lambda_{\text{in}}^{-1}}{dqd\omega} = \frac{\hbar}{\pi a_0 E}\,\text{Im}\left\{\frac{-1}{\varepsilon(q,\omega)}\right\}\frac{1}{q}, \tag{5}$$

where λ_{in} is the electron inelastic mean free path, the average distance that an electron can travel in the material before losing energy; a_0 is the Bohr radius, $\hbar q$ and $\hbar\omega$ are the momentum transfer and the energy loss, respectively. The energy loss function, defined as $\text{Im}\{-1/\varepsilon\}$, is a vital quantity to describe the response of the medium to the disturbance of an external electron and, thus, completely determinesthe behavior of electron inelastic scattering in a specific material. However, except for a free electron gas (Al is a typical example of a nearly free electron metal) whose dielectric response can be well described by the Lindhard dielectric function,[57] for other materials, there are several dielectric function models. Even though all these models employ the experimental measured optical constants, which largely specify the behavior of the dielectric response at a long wavelength limit ($q \to 0$), their extensions into the finite momentum transfers vary. Therefore, the dielectric function model plays another role of uncertainty factor in a Monte Carlo simulation. In this study, we have employed three dielectric function models: (1) the Levine and Louie model (LLM),[58] (2) the full Penn's algorithm (FPA),[57] and (3) the super-extended Mermin algorithm (SMA).[59] The FPA and SMA are useful for metals, while the LLM is an extension to semiconductors and insulators having a bandgap. The Drude-type oscillator terms used in the SMA were obtained by fitting to the experimental optical energy loss function data at the optical limit $q \to 0$,[55] where the Mermin-type oscillator terms agree with the Drude-type oscillators. While for both the FPA and LLM, the optical energy loss function data are directly used without the aid of oscillator terms.

When an inelastic scattering occurs, the energy loss $\hbar\omega$ and momentum transfer $\hbar q$ are determined by a random sampling from the double differential inverse inelastic mean free path,[6] Eq. (5). The cascade electron is assumed to be excited from the valance band; the excitation probability is proportional to the joint density of states of a free electron material, i.e., $p(E', \hbar\omega) \propto \sqrt{E'(E' + \hbar\omega)}$, where E' is the energy of the electron in the valance band measured from the bottom of the valence band. Then the kinetic energy of the generated secondary electron is $E_s = E' + \hbar\omega - (E_v + E_g)$, where E_v is the width of the valence band and E_g is the bandgap. The energy reference level of the generated secondary electron in the material is set at the bottom of the conduction band. The direction of the cascade electron is along the direction of momentum transfer $\hbar q$.

D. Optical energy loss function data

The linescan profile is entirely related to the secondary electron signals, while the cascade secondary electrons are generated in the inelastic scattering events. Therefore, the optical energy loss function data, $\text{Im}\{-1/\varepsilon(q = 0, \omega)\}$, is an essential input to a Monte Carlo simulation of the linescan profile. The optical dielectric function, $\varepsilon(\omega) = \varepsilon_1(\omega) + i\varepsilon_2(\omega)$, can be derived from the optical constants, i.e., the refractive index $n(\omega)$ and extinction coefficient $k(\omega)$: $\varepsilon_1 = n^2 - k^2$, $\varepsilon_2 = 2nk$. Palik has compiled the measured optical constants by optical methods from low to high photon energies, $\hbar\omega$, for some elements and compounds from many sources into a database.[60] However, even in the same photon energy range, the measured optical energy loss function data by different researchers may differ. Therefore, the optical energy loss function data as a necessary input to a Monte Carlo simulation may act as an uncertainty factor to impact the simulated linescan profile.

For Si, as the material considered in this study, we have attained three combined optical energy loss function datasets (Fig. 4 in Ref. 55). They are named "crystal (Palik)," "crystal (Yang)," and "doped (Palik)" by combining several sources from Palik,[60] Henke *et al.*,[61,62] and Yang *et al.*[63,64] For the Sb-doped (at concertation of ∼0.002) n-type Si, the energy loss function is much enhanced below the bandgap as compared with that of pure Si. Limited by the energy resolution of the electron beam technique, the energy loss function in the "crystal (Yang)" dataset below 2 eV was approximated by a straight line such that the sum rules are satisfied. Therefore, all the energy loss functions for crystalline silicon (c-Si) are very close in value above the bandgap, and their difference is mainly at the phonon excitation part below the bandgap. To find the accuracy of these energy loss functions, we have used two sum rules, called the oscillator strength sum rule (*f*-sum rule) and perfect screening sum rule (*ps*-sum rule), for the verification of the three energy loss function datasets.[64] Each sum rule reinforces the respective energy region of importance and, therefore, these sum rules present a simple overall estimation for the accuracy of the energy loss function.[55]

E. Work function data

After certain elastic and inelastic collisions inside the sample, an electron may arrive at the surface for emission, and the refraction or reflection of the electron from the surface will be judged by a quantum mechanical transmission coefficient[65] as

$$T(E,\beta)=\begin{cases}\dfrac{4\sqrt{1-U_0/E\cos^2\beta}}{\left[1+\sqrt{1-U_0/E\cos^2\beta}\right]^2}, & \text{if } E\cos^2\beta > U_0,\\ 0, & \text{otherwise,}\end{cases} \tag{6}$$

where β is the angle between the direction of a moving electron and surface normal and U_0 is the surface potential barrier. An electron gains or loses its kinetic energy by the potential barrier when penetrating the surface from the vacuum side or the bulk side, respectively. Hence, the surface barrier plays a significant role in secondary electron emission. When the energy reference level in the material is set at the bottom of the valence band, $U_0 = E_F + W$ for a metal[6,44,66] and $U_0 = E_v + E_g + \chi$ for a semiconductor or an insulator, where E_F is the Fermi energy, W is the work function, E_v is the width of the valence band, E_g is the bandgap, and χ is the electron affinity. While in the present study, the energy reference

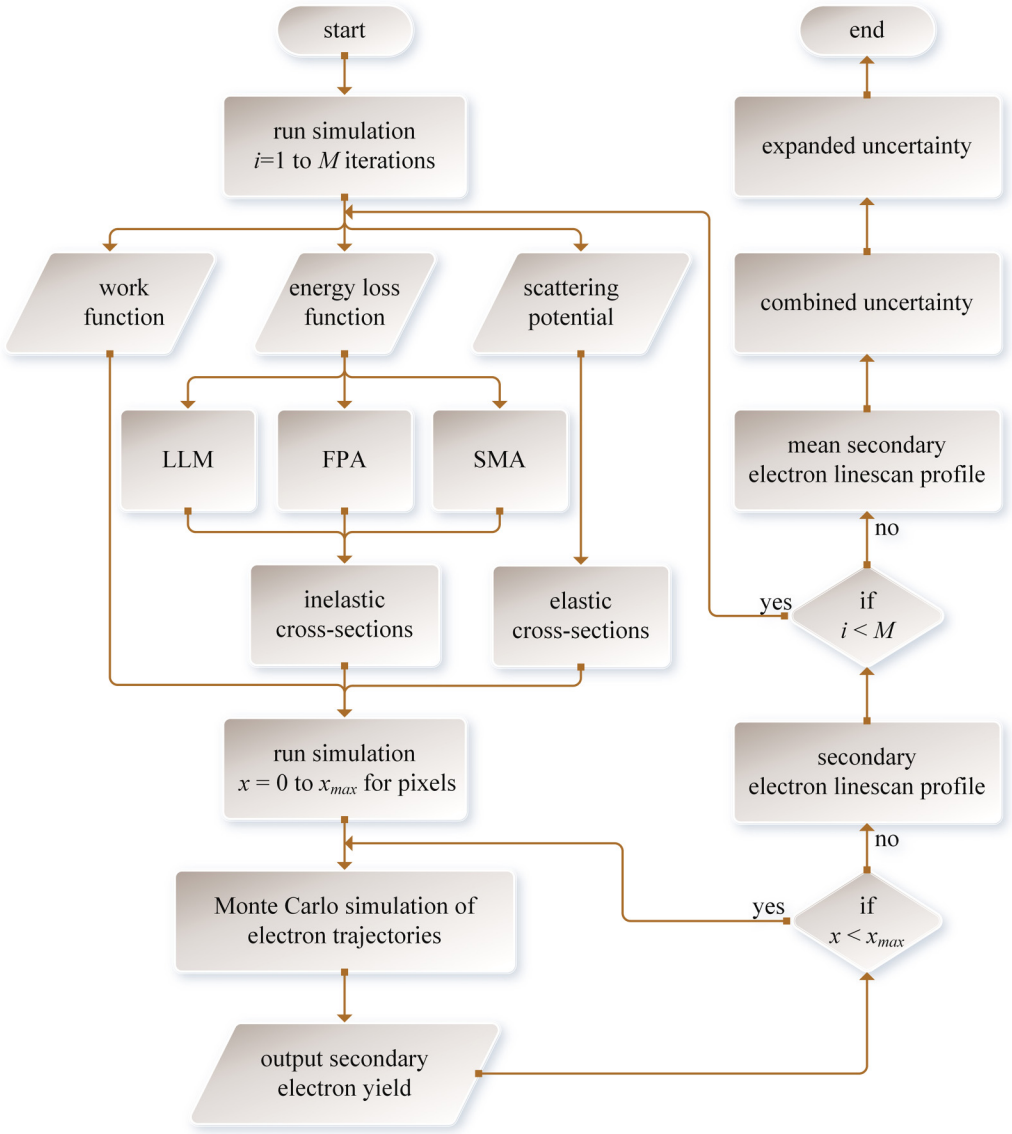

FIG. 2. Flowchart for estimating uncertainty of the linescan profiles by a Monte Carlo simulation method, where the dielectric function models used are the LLM, FPA, and SMA.

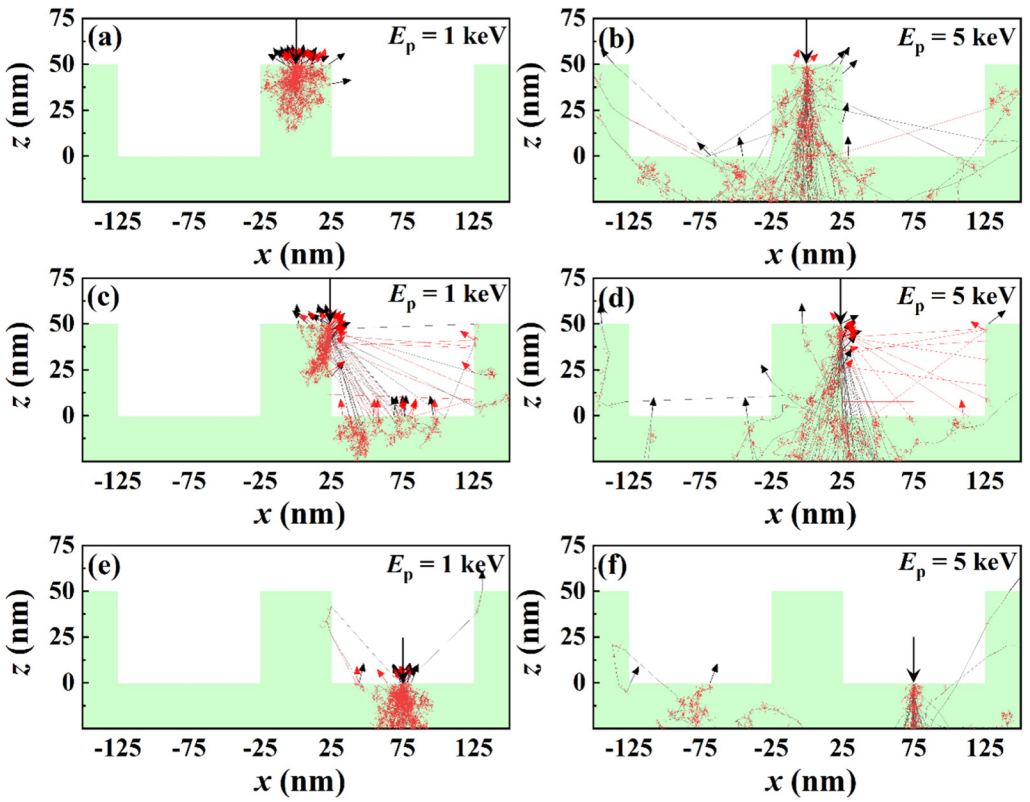

FIG. 3. Scattering trajectories of 50 primary electrons (black) and their generated cascade secondary electrons (red) nearby a rectangle Si line structure. The black and red arrows indicate the emitted backscattered and secondary electrons. The electron beam of the size of FWHM = 1 nm is normally incident onto (a) and (b) the mid of the top surface, (c) and (d) the top edge and (e) and (f) the mid of the bottom substrate surface. Whereas primary energy is (a), (c) and (e) 1 keV and (b), (d), and (f) 5 keV.

level of an electron is set as the vacuum level in the vacuum, and the lowest unoccupied state inside the material [i.e., the Fermi level for metals ($U_0 = W$) or the bottom of the conduction band for semiconductors and insulators ($U_0 = \chi$)[67]]. Since the Fermi level of a semiconductor is at the mid of energy gap at room temperature, the electron affinity measured from the bottom of the conduction band to the vacuum level is $\chi = W - E_g/2$. For Si, $E_g \simeq 1.1$ eV and $E_v \simeq 12.5$ eV.

There are several methods for the experimental determination of the work function, i.e., the thermionic method, the photoelectric method, the field-emission method, the effusion method, the contact potential difference method, and the calorimetric method. For Si, the available data of the work function and electron affinity χ measured by different researchers under different experimental conditions are listed elsewhere.[55] Experimentally, the biggest source of the measured secondary electron yield data comes from surface contamination and surface roughness. In our present approach, we have considered part of the contamination effect with the factor of work function. The reported range of the measured W is from 3.59 to 5.4 eV,[68–81] and we used this range for our uncertainty evaluation in the simulation.

III. MONTE CARLO UNCERTAINTY QUANTIFICATION

The combined uncertainty in a simulation due to the uncertain variables can be derived analytically if a functional expression of these variables is given. For example, for a function $y = f(x_1, x_2, \ldots, x_N)$, the combined standard uncertainty for the measurand y can be determined as $u_y^2 = \sum_{i=1}^{N} (\partial f/\partial x_i)^2 u_{x_i}^2$, where u_{x_i} is the uncertainty due to the ith input quantity.[82] However, in the present case, the functional dependence of electron emission yields on the uncertainty variables (i.e., scattering potential model, dielectric function model, energy loss function data, and work function data) cannot be explicitly given. Therefore, we have adopted a Monte Carlo uncertainty quantification approach to evaluate the propagation of uncertainties. For this, one has to first set the probability density functions for the input quantities and then execute a Monte Carlo simulation process for a certain number of times. The simulation will provide the distribution of the output and, hence, the uncertainty of the output. In this study, the Monte Carlo uncertainty procedure is just the Monte Carlo simulation process of secondary electron emission with different combinations of the selected uncertainty variable values.

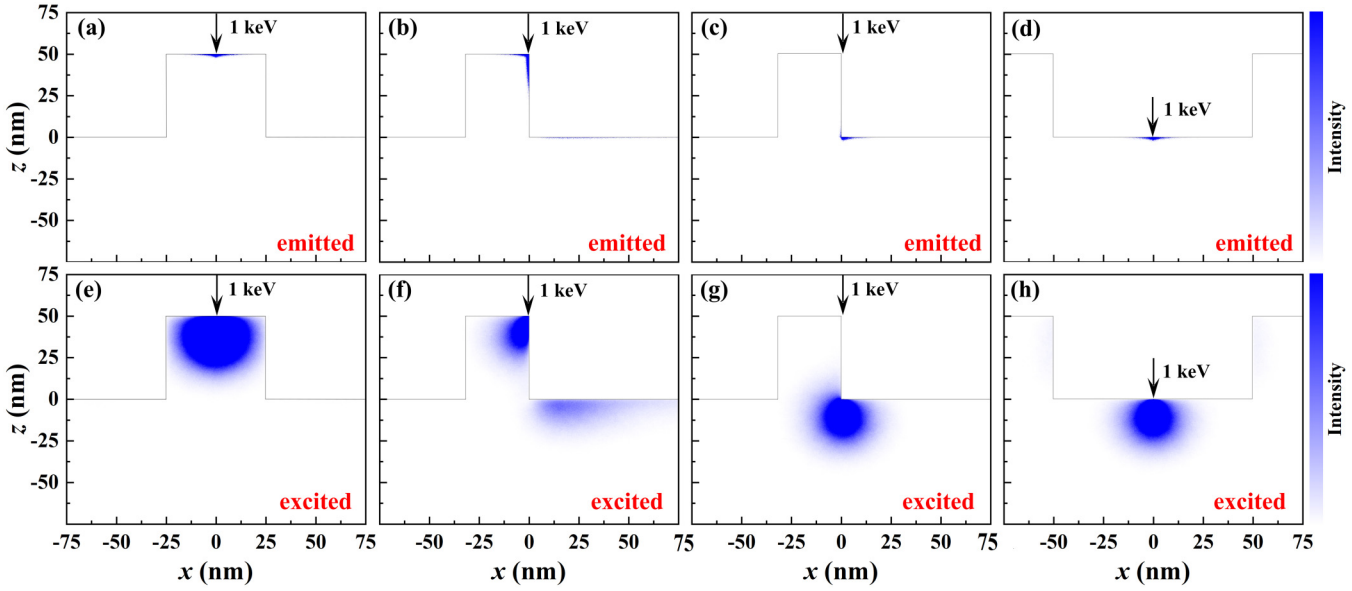

FIG. 4. Simulated spatial density distributions of the internal population of cascade secondary electrons at their birth sites in a rectangle Si line structure for different incident positions of 1 keV incident electron beam at normal incidence. The top panel (a)–(d) is for the emitted secondary electron signals in SEM imaging and the bottom panel (e)–(h) is for all the generated secondary electrons. The beam incident positions are (from left to right): the mid of the top surface, the top edge, the bottom edge, and the mid of the bottom substrate surface.

Figure 2 demonstrates the flow chart for the present theoretical calculation of secondary electron emission and the related uncertainty quantification. Uncertain inputs of the material properties involve work function and energy loss function, while uncertainty for the theoretical modeling includes the elastic scattering potential and the dielectric function model. Here, we have considered that all the uncertain inputs are equally important and uniformly distributed. Then, several Monte Carlo trials, $M = 17280$ (a combination of 384 scattering potentials, 3 dielectric function models, 5 work function values, and 3 energy loss function datasets) for each incident energy are chosen priori. We have employed a parallel computer to perform the Monte Carlo calculation, which is very suitable for our present purpose of uncertainty quantification. For each simulation, we have traced 1×10^5 incident electron trajectories and several dozens of cascade secondary electron trajectories.

IV. RESULTS AND DISCUSSION

Figure 3 demonstrates the simulated electron trajectories, including incident electrons and their generated cascade electrons near a rectangle Si line structure surface. The primary beam at the beam size (measured by the full width at half maximum, FWHM) of 1 nm and the energy of 1 and 5 keV is incident onto either the top surface, the edge, or the substrate of the Si line structure. One can observe that at a higher energy, 5 keV [Figs. 3(b), 3(d), and 3(f)], the incident electrons can penetrate much deeper inside the structure than at a lower energy, 1 keV [Figs. 3(a), 3(c), and 3(e)]. While secondary electrons are produced more widely in the lateral direction at the lower energy, representing the stronger neighboring effect. When the primary beam is incident at an edge side of the Si line structure [Figs. 3(c) and 3(d)], more secondary electrons are emitted from the edge and nearby surfaces, while in the case of the beam incident at the substrate position [Figs. 3(c) and 3(f)], the secondary electron emission is more local and depressed due to the absorption by the nearby structure.

Figure 4 compares the spatial density distribution of the internal population of cascade secondary electrons at their birth sites between the different incident positions of an electron beam of 1 keV. The top panel shows the distributions for the emitted secondary electrons and the bottom panel for the spatial distributions of all the generated secondary electrons. This figure more clearly illustrates the varied local emission properties of secondary electrons when the beam is incident at different positions. At the top and bottom substrate surfaces [Figs. 4(a) and 4(d)] the secondary electrons are only emitted from the region around the incident position within a depth of ~1 nm. When the incident position is at the top edge [Fig. 4(b)], many secondary electrons can be emitted not only from the top surface and the side surface but also some from the bottom substrate surface far away from the incident location; hence, the so-called edge effect for the edge blooming intensity is produced. When the incident position is at the bottom edge [Fig. 4(c)], the fraction of emission from the line structure (the left part in the figure) is attenuated compared to the planar surface case, producing the edge bottom dip in the linescan profile of secondary electron intensity.

Figure 5 shows the effect of the variation of work function value on the calculated linescan profile of the Si rectangle line structure. Here, we deal with a rather ideal experimental condition,

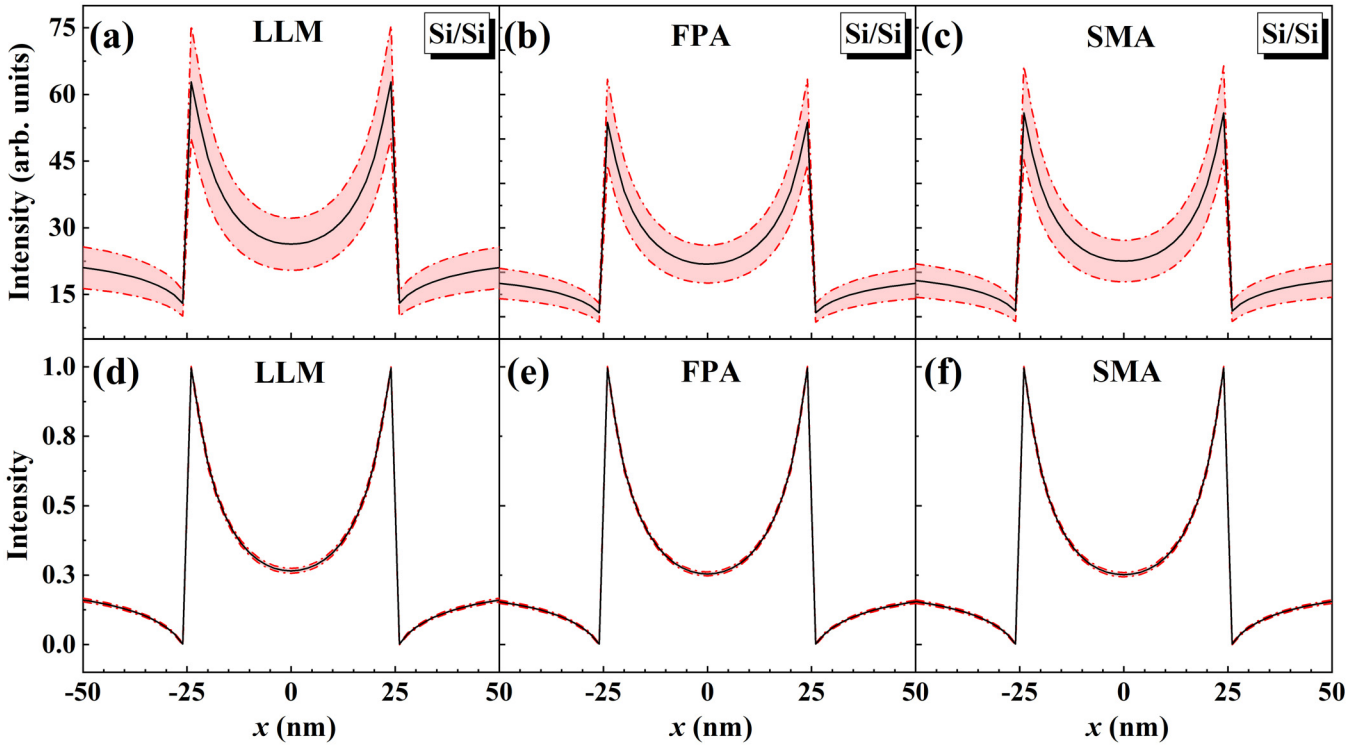

FIG. 5. Simulated linescan profiles of a rectangle Si line structure on a Si substrate for a variation of work function in the range of 3.59–5.41 eV by using the (a) and (d) LLM, (b) and (e) FPA, and (c) and (f) SMA. Whereas the bottom panel [(d)–(f)] shows the mean and the standard deviation of the normalized linescans by the peak maximum. The black line represents the mean profile, and the red-shaded region represents standard deviations. The elastic scattering potential = "No. 42 001" and energy loss function = "crystal (Palik)." In these Monte Carlo simulations, an electron beam of 1 keV at the beam size (FWHM) of 0 nm is normally incident and 1×10^5 incident trajectories are used for each incident position.

that is, the maximum edge effect with the sharpest edge shape and the smallest electron beam size by considering that the experimental probe size for a nanowire LaB_6 field-emission electron gun is ~2 nm.[83] In Monte Carlo simulations, the number of incident trajectories, $N_p = 1 \times 10^5$, is used for each incident position of each linescan profile. Therefore, the statistical fluctuation of simulated secondary electron signal intensity can be estimated as $1/\sqrt{N_s} = 1/\sqrt{N_p\delta} \sim 0.6\%$, where N_s is the number of emitted secondary electrons with energies less than 50 eV and δ is the secondary electron yield (which represents the ratio of the number of emitted secondary electrons to the number of incident primary electrons), where $\delta \sim 0.3$ at 1 keV.[55] This fluctuation for the Monte Carlo computation uncertainty is so small and can be omitted. The linescan profiles were simulated 10 000 times by changing the work function value according to the uniform distribution and for all the FPA, SMA, and LLM. In Fig. 5 the black line represents the mean linescan profile and the red-shaded region represents the standard deviation of linescans due to the change of work function. The edge blooming and the edge bottom dip are clearly seen in the linescan profile for the reason stated above. All three dielectric function models produce a similar linescan profile shape, except the intensities are somewhat different. The work function also changes the emission intensity [Figs. 5(a)–5(c)] but not the shape of the normalized linescan profile [Figs. 5(d)–5(f)] because the low energy secondary electrons are sensitive to the value of the work function when passing through the potential barrier of the surface where they lose energy. One may observe that the standard deviation of the intensity is the vastest in the middle region of the line structure.

The CD estimation in this study is performed accordingly as follows: we define CD_1 to be the distance between the two peak maxima, and CD_3 to be the distance between the two valley minima in a linescan profile. Then CD_2 is taken as the mean of CD_1 and CD_3. It should be noted that in the simulation, the line structure is specified and the structure size is given; what we measured as the CD value here is the size from the simulated linescan profile. For a rectangle line structure, CD_2 should be quite close to the CD value in the line structure modeling. In the following, we have also considered other sidewall angle cases: 80° and 100°, while in structure modeling, we keep the CD at the mid height of these two line structures to be the same value, 50 nm, as in the rectangle case. However, it should be noted that this simple peak/valley estimation method of the CD cannot be accurate as it ignores the

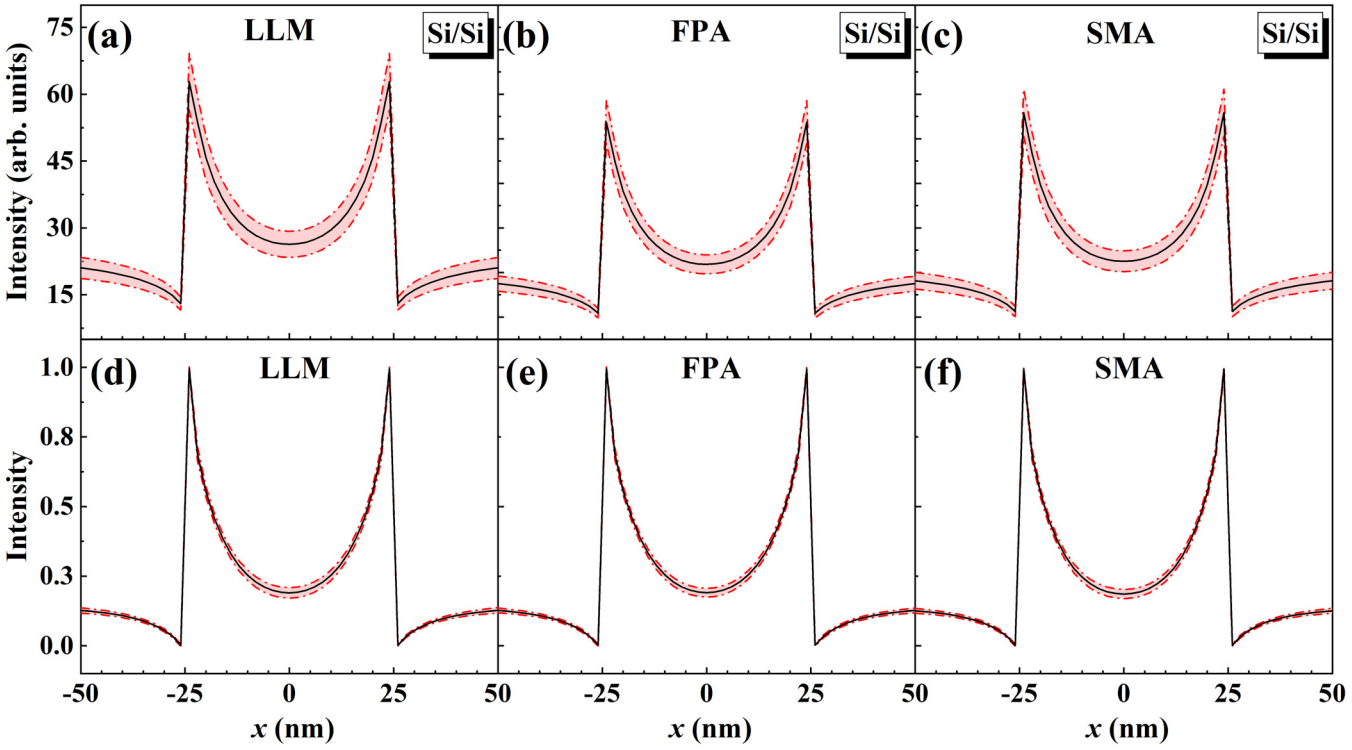

FIG. 6. (Top panel) Simulated linescan profiles of a rectangle Si line structure on a Si substrate for a variation of elastic scattering potential, and using the (a) LLM, (b) FPA, and (c) SMA. (bottom panel) the mean and standard deviation of the normalized linescans by the peak maximum for a variation of elastic scattering potential by using the (d) LLM, (e) FPA, and (f) SMA. The black line represents the mean profile and the red-shaded region represents standard deviations. The work function is 4.61 eV and the energy loss function = "crystal (Palik)." In these Monte Carlo simulations, an electron beam of 1 keV at the beam size (FWHM) of 0 nm is normally incident and 1×10^5 incident trajectories are used for each incident position.

linescan shape, which contains much more information on the line structure than the peak/valley position. A reasonable estimation should be done with the MBL method.[37] However, for our present purpose of uncertainty estimation, we focus on the CD variation (i.e., the standard deviation) value, but not the absolute CD value; therefore, this definition of mean CD (i.e., CD_2) is convenient for the evaluation of uncertainty.

Figure 6 shows the effect of the elastic scattering potential on the simulated linescan profiles. Here, 384 potential models are used and the corresponding elastic scattering cross section files are provided as input to the Monte Carlo simulation. All of these elastic scattering potentials are considered to be equally important. From the figure, one may find that the elastic scattering cross section also influences, to some extent, the secondary electron emission intensity, but, not the linescan shape. For this rectangle line structure of the side length of 50 nm, CD_1 and CD_3 estimated are 48 and 52 nm, respectively, which are the same for the three dielectric function models. Hence, CD_2 is obtained as the modeling value, 50 nm.

Figure 7 illustrates the influence of the energy loss function dataset on the linescan profiles. It is evident from Fig. 7(a) that the LLM dataset has a negligible effect on the emission yield because all the differences in the different energy loss functions below the bandgap have been removed in the LLM. While in the FPA and the SMA, the energy loss function dataset has a small effect. In addition, the LLM produces more secondary electrons than the other two models because the electrons cannot have energy loss below the bandgap, i.e., phonon excitation is omitted. Nevertheless, neither the CD measurement is found to be influenced by the electron inelastic mean free path calculation method via the dielectric function model nor by the calculated electron inelastic mean free path values via the energy loss function dataset.

Figures 8(a)–8(c) show the final evaluated mean linescan profiles for the line structures with different sidewall angles, i.e., 80°, 90°, and 100°, from the Monte Carlo simulations together with the uncertainty (standard deviation),

$$u_I = \sqrt{\sum_{i=1}^{M} (I_i - \bar{I})^2/(M-1)}, \tag{7}$$

where I_i represents the intensity of secondary electrons emitted from the ith scanning position, and $\bar{I}$ represents the mean value. At

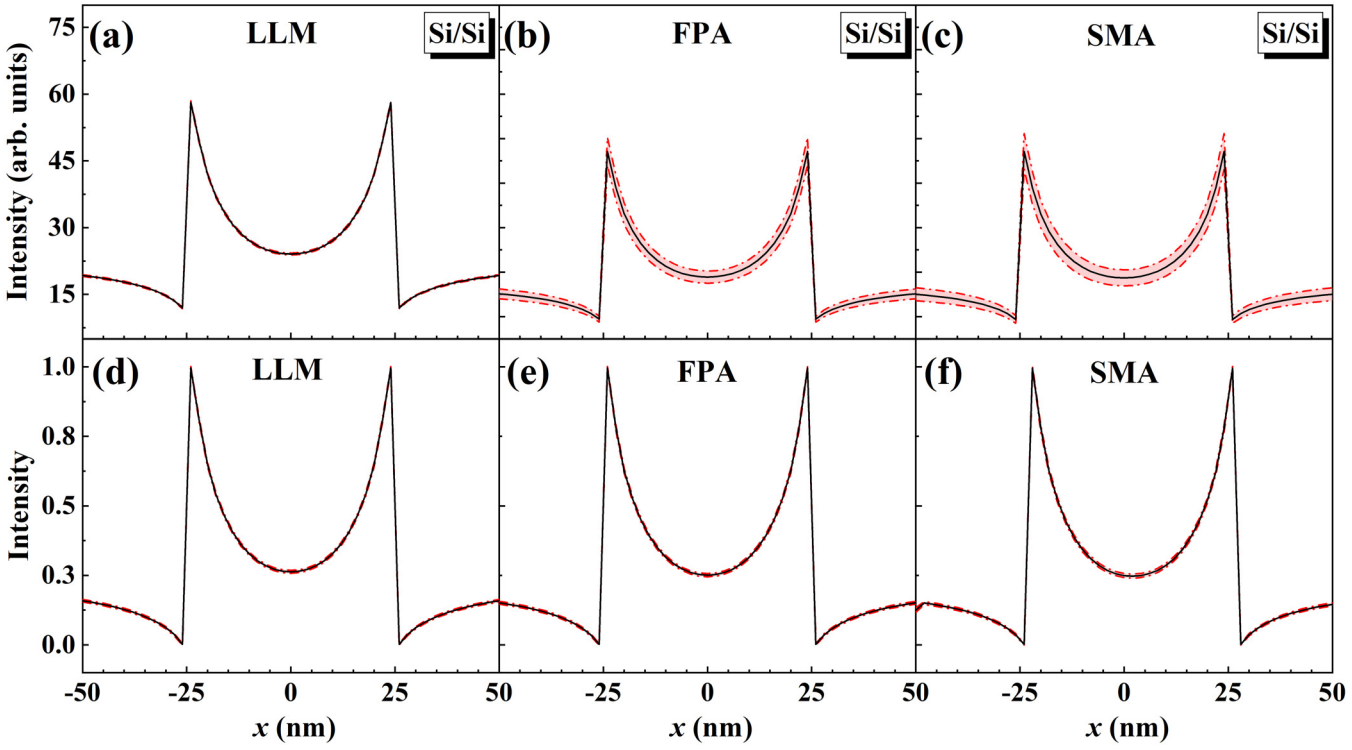

FIG. 7. (Top panel) Simulated linescan profiles of a rectangle Si line structure on a Si substrate for a variation of energy loss function dataset and using the (a) LLM, (b) FPA, and (c) SMA. (bottom panel) The mean and standard deviation of the normalized linescans by the peak maximum for a variation of energy loss function dataset by using the (d) LLM, (e) FPA, and (f) SMA. The black line represents the mean profile and the red-shaded region represents the standard deviation. The work function is 4.61 eV and the elastic scattering potential = "No. 42 001." In these Monte Carlo simulations, an electron beam of 1 keV at the beam size (FWHM) of 0 nm is normally incident and 1×10^5 incident trajectories are used for each incident position.

each scanning point, the calculations are performed over a total number of $M = 17280$ Monte Carlo simulations by changing an input. Figures 8(d)–8(f) show all these 17 280 linescan profiles simulated for the line structures with different sidewall angles, i.e., 80°, 90°, and 100°, respectively, from which we have estimated CD_1, CD_3 and, hence, CD_2 for each linescan profile. The associated CD uncertainty (standard deviation) is given similarly by

$$u_d = \sqrt{\sum_{i=1}^{M} (d_i - \bar{d})^2/(M-1)}, \tag{8}$$

where d represents the estimated CD_1, CD_2, or CD_3 and $\bar{d}$ represents the mean value. Two x-grid intervals are used to reduce computation: a coarse grid of 2 nm for intensity uncertainty evaluation with Eq. (7) as shown in the main frame of Figs. 8(a)–8(f), and a fine grid of 0.1 nm for the CD uncertainty evaluation with Eq. (8) as shown in the insets of Figs. 8(g)–8(l). Figures 8(a)–8(f) and 8(g)–8(l) emphasize on the intensity change and the shape change of the linescan profiles, respectively. It is shown in Figs. 8(a)–8(c) that the relative intensity uncertainties at the mid of the top surface, $u_{I_{(0\text{ nm})}}/I_{(0\text{ nm})}$, are 0.30, 0.26, and 0.29, respectively, for the sidewall angles of 80°, 90°, and 100°, and the ones at an edge, $u_{I_{(25\text{ nm})}}/I_{(25\text{ nm})}$, are 0.21, 0.22, and 0.24, respectively. For normalized linescan profiles, they are $u_{I_{(0\text{ nm})}}/I_{(0\text{ nm})} = 0.13$, 0.10, and 0.14 for the sidewall angles of 80°, 90°, and 100°, respectively. Therefore, it is seen that although the secondary electron intensity does change with physical parameters in a Monte Carlo modeling, the shape of the linescan profile varies very slightly.

From Table I, one can see that the standard deviation of CD_1 is always greater than that of CD_3 and, hence, that of CD_2 has a value in between. The averaged CD_2 for the line structures with sidewall angles of 80°, 90°, and 100° are, respectively, 49.9, 49.6, and 57.7 nm with the standard derivation of 0.06, 0.15, and 0.24 nm. Then in this limited investigation of simple structure geometry, the estimated CD_2 is very close to the modeling value of 50 nm with a negligible standard deviation for sidewall angles smaller than 90°. But, for sidewall angles greater than 90°, the estimated CD_2 is far from the true value. In addition, by considering other factors like the edge angle, the estimated CD_2 may further differ from the modeling value of the line width; this is exactly the reason to use the MBL method other than the simple peak/valley method. However, even though the CD evaluation may be

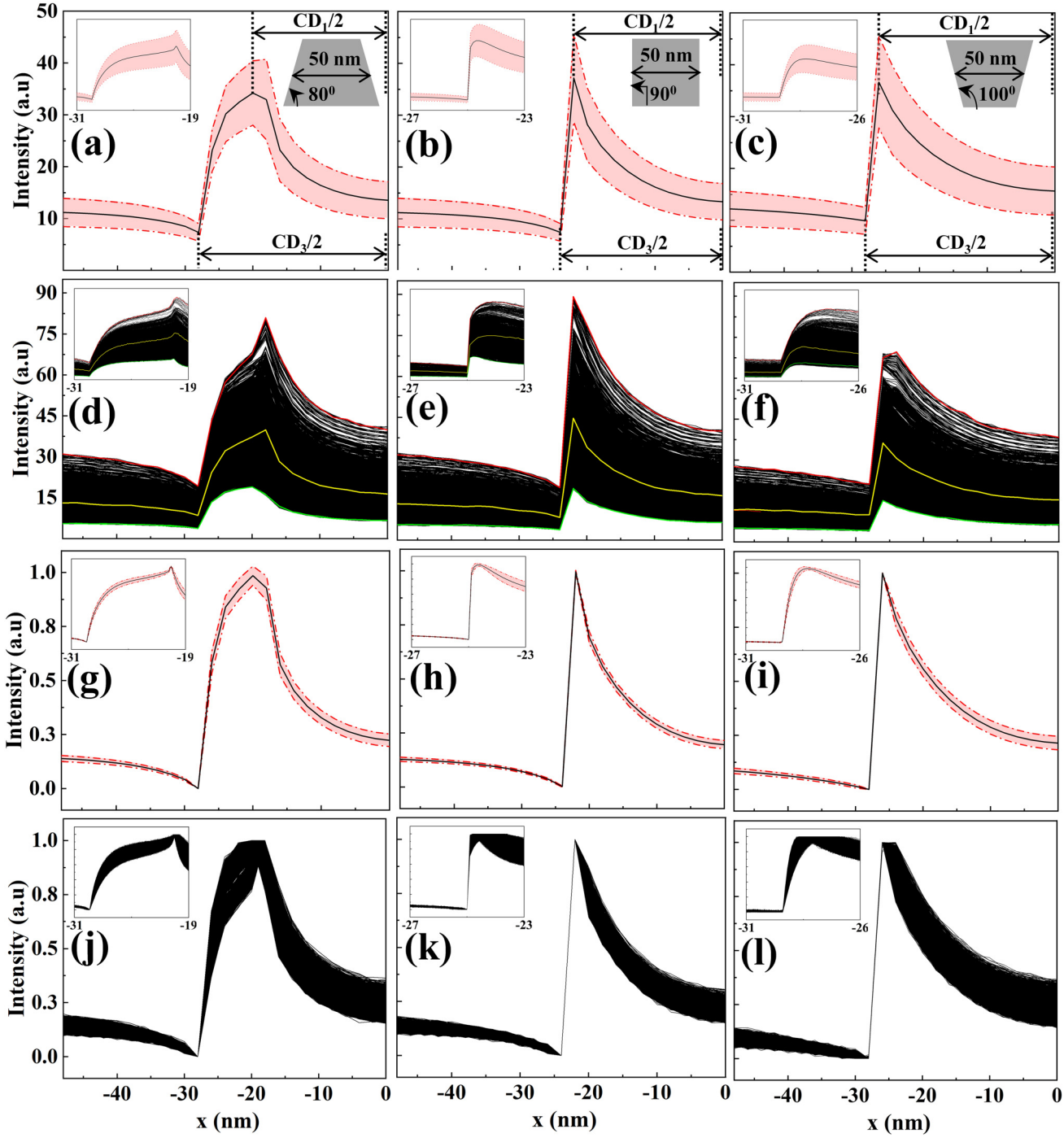

FIG. 8. (a)–(c) The mean (black line) of the simulated linescan profiles together with the standard deviation (red-shaded region) for a Si line structure on a Si substrate. (d)–(f) All the simulated 17 280 linescan profiles by taking every considered theoretical uncertainty into account, where the red, yellow, and green lines represent three individual linescans for visual clarity. (g)–(i) The mean (black line) of the normalized linescan profiles by the peak maximum together with the standard deviation (red-shaded region). (j)–(l) All the normalized 17 280 linescans. The inset shows the linescan profiles near an edge. The *x*-grid intervals are 0.1 and 2 nm for the inset and the main frame, respectively. The sidewall angle of the Si line structure is (a), (d), (g), and (j) 80°; (b), (e), (h), and (k) 90°; (c), (f), (i), and (l) 100°. In these Monte Carlo simulations, an electron beam of 1 keV at the beam size (FWHM) of 0 nm is normally incident and 1×10^5 incident trajectories are used for each incident position.

TABLE I. The evaluated CD values and their standard deviations for Si line structures at different sidewall angles calculated with 17 280 linescan profiles.

Sidewall angle	CD	Min (nm)	Max (nm)	Mean (nm)	Standard deviation (nm)
80°	CD_1	40.0	41.2	41.0	0.13
	CD_2	49.4	50.0	49.9	0.06
	CD_3	58.6	58.8	58.8	0.01
90°	CD_1	47.2	49.6	49.2	0.31
	CD_2	48.6	49.8	49.6	0.15
	CD_3	50.0	50.0	50.0	0.00
100°	CD1	54.0	57.6	56.5	0.48
	CD_2	56.4	58.2	57.7	0.24
	CD_3	58.8	60.2	58.8	0.02

inaccurate, the standard derivation is still negligible. This result indicates that by taking every considered theoretical uncertainty into account, all the obtained CDs with the simple peak/valley method are quite the same within the accuracy, in comparison to the grid precision, 0.1 nm. Hence, the estimated CD values are negligibly related to the physical factors in a Monte Carlo modeling as the present Monte Carlo theoretical framework is concerned; it is evident that CDs rely more critically on the line structure and electron beam parameters. However, it should be also pointed out that by considering the fact that the MBL method is shape-sensitive and the insets of Figs. 8(g)–8(i) show that the shape of a normalized linescan curve varies only slightly with modeling, the use of the MBL method in CD evaluation may thus give slightly different results, which means that when an experimental linescan profile is measured, the use of different MBL database built with different Monte Carlo physical modeling may result in slightly different CD values. Therefore, according to ISO-21466, the modeling parameters should be specified when building a MBL database.

It is also necessary to mention that the qualitative conclusion for the present results obtained for a Si line structure on a Si substrate should be also valid for a Si line structure on other substrates, e.g., TiN. This is because the effect of the substrate mostly contributes only to the background intensity but cannot change significantly the shape of the linescan curve near the line edge. Considering the fact that TiN or other similar semiconductor materials have a similar secondary electron yield curve as Si,[84] then the substrate effect is even less. Furthermore, the present Monte Carlo physical modeling is limited to the up-to-date model, which is the combination of Mott's electron elastic scattering cross section and dielectric function formulation for electron inelastic scattering cross section; the old-fashioned Monte Carlo physical modeling with the use of Rutherford's electron elastic scattering cross section and stopping power-based approach to electron inelastic scattering has been known inaccurate to low energy secondary electrons. Other geometrical factors, such as the aspect ratio and the spacing between the lines, have no obvious effect on the present observations. Logically, modeling physical factors are independent of the geometrical factors like the sidewall; therefore, the CD determination, considering these geometrical factors, should present a standard deviation no greater than that of the sidewall as given in Table I.

According to the ISO-JCGM 100,[82] the following parameters should be reported as the measurement data: (i) an estimation of the output quantity, taken as the mean values generated; (ii) the standard uncertainty, taken as the standard deviation of these generated values; (iii) the chosen coverage probability or the level of confidence (usually 95%), and (iv) the endpoints corresponding to the selected coverage interval. The last step of uncertainty quantification is about the expanded uncertainty at the k% level of confidence, i.e.,

$$U_{\%} = k_{\%} u, \tag{8}$$

where the values of $k_{\%}$ at 95% and 75% confidence levels are $k_{95} = 1.96$ and $k_{75} = 1.16$, respectively. Figure 9 shows the expanded uncertainty plots for the calculated linescan of the line

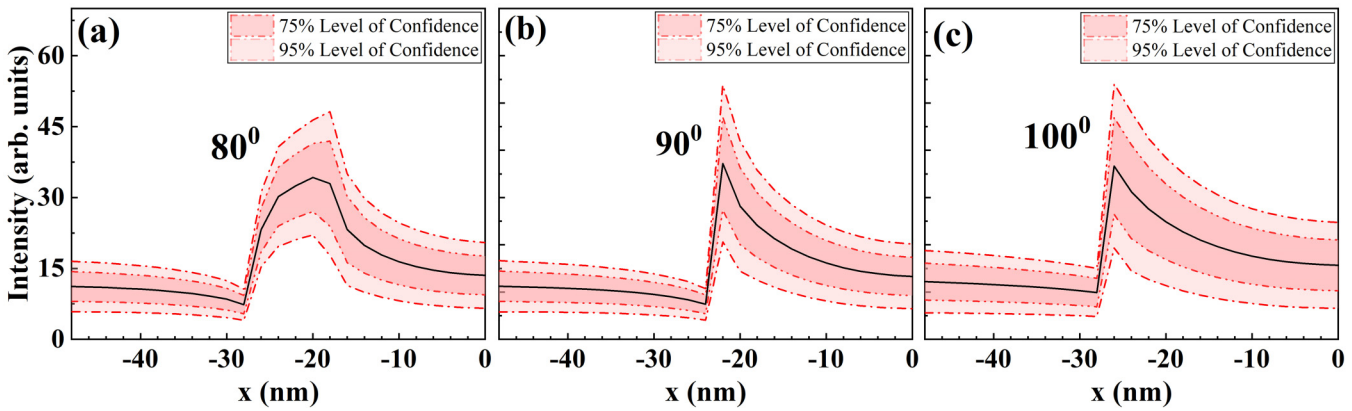

FIG. 9. Simulated mean linescan profile (black line) together with the expanded uncertainties at 75% (dark red) and 95% (light red) level of confidence for a Si line structure having sidewall angles (a) 80°, (b) 90°, and (c) 100° placed on a Si substrate. The electron beam of 1 keV at the beam size (FWHM) of 0 nm is normally incident. In the Monte Carlo simulations, 1×10^5 incident trajectories are used for each incident position.

structure having different sidewall angles at 95% (light red) and 75% (dark red) levels of confidence. One may also observe that the calculated uncertainty in the linescan profiles of the Si line structure due to different factors hardly affects the CD measurement.

Although the present study provides an insight into the influence of theoretical input parameters on CD measurements with the CD-SEM by using the Monte Carlo simulation techniques, it is also necessary to acknowledge the limitations of this study. First, we focused on the fixed experimental morphology and beam parameters throughout our simulation process, neglecting the potential variations that occur in real-world scenarios. This simplified approach allowed us to isolate the effects of theoretical inputs from the CD measurements, but may not fully reflect the complexities in practical applications. Second, our study primarily examined the impact of simulation procedures and theoretical inputs, potentially overlooking other sources of uncertainty that could arise from sample preparation, instrument calibration, and other systematic errors. To address these limitations and provide a more comprehensive understanding of the CD measurements, we plan to conduct an experimental study in the near future. This forthcoming study will involve utilizing a field-emission SEM instrument equipped with a nanotube LaB_6 electron gun to investigate the influence of beam parameters on CD measurements. By incorporating the experimental data and considering a wider range of uncertainty factors, we aim to further enhance the accuracy and reliability of CD-SEM metrology.

Overall, our present study serves as a foundation for future research, emphasizing the importance of both theoretical inputs and the related experimental factors in CD measurements. We hope that our findings would inspire further investigations into the optimization of CD measurement techniques, ultimately advancing dimensional metrology in the semiconductor industry and facilitating more precise manufacturing processes.

V. CONCLUSIONS

In this study, we have used the Monte Carlo uncertainty quantification procedure to investigate the uncertainty of CD measurement due to the involved uncertain theoretical modeling factors. We demonstrate that the uncertain theoretical factors, including the work function, elastic scattering potential model, dielectric function model, and energy loss function dataset, in the Monte Carlo simulation of a CD-SEM linescan profile, have a negligible effect on the CD measurement, even though they impact secondary electron emission intensity. Therefore, the CD measurement uncertainty by the peak/valley method is more critically related to the geometric and beam parameters, while the accurate measurement should be done by the MBL method.

ACKNOWLEDGMENTS

We thank Professor H. M. Li and the supercomputing center of USTC for the support of parallel computing. S. F. Mao acknowledges the National MCF Energy R&D Program of China (Grant No. 2019YFE03080500) and the Collaborative Innovation Program of Hefei Science Centre, CAS (Grant No. 2022HSC-CIP010). Y. B. Zou acknowledges the Natural Science Foundation of Xinjinag Uygur Autonomous Region (Grant No. 2022D01A223). Y. G. Li acknowledges the National Natural Science Foundation of China (Grant No. 11975018), the National Magnetic Confinement Fusion Energy Research Project (Grant No. 2018YFE0308100), and the Youth Innovation Promotion Association of CAS (Grant No. Y202087). B. Da acknowledges the Kurata Grants from The Hitachi Global Foundation and the Iketani Science & Technology Foundation. Z. J. Ding is supported by the Chinese Education Ministry through "111 Project 2.0" (No. BP0719016). M. S. S. Khan acknowledges CAS-TWAS President's fellowship.

AUTHOR DECLARATIONS

Conflicts of Interest

The authors have no conflicts of interest to disclose.

Author Contributions

M. S. S. Khan: Data curation (equal); Formal analysis (equal); Investigation (equal); Visualization (equal); Writing – original draft (equal); Writing – review & editing (equal). **S. F. Mao:** Methodology (equal); Software (equal). **Y. B. Zou:** Funding acquisition (equal); Software (equal). **Y. G. Li:** Conceptualization (equal); Methodology (equal); Software (equal). **B. Da:** Methodology (equal); Software (equal). **Z. J. Ding:** Conceptualization (equal); Formal analysis (equal); Funding acquisition (equal); Methodology (equal); Project administration (equal); Software (equal); Supervision (equal); Writing – review & editing (equal).

DATA AVAILABILITY

The data that support the findings of this study are available from the corresponding author upon reasonable request.

REFERENCES

[1]K. F. J. Heinrich, D. E. Newbury, and H. Yakowitz, in *Use of Monte Carlo Calculations in Electron Probe Microanalysis and Scanning Electron Microscopy* (US Department of Commerce, National Bureau of Standards, 1976).
[2]J. Schou, P. Kruit, and D. E. Newbury, *Fundamental Electron and Ion Beam Interactions with Solids for Microscopy, Microanalysis and Microlithography* (Scanning Microscopy International, 1991).
[3]R. Shimizu, "Quantitative analysis by auger electron spectroscopy," Jpn. J. Appl. Phys. **22**, 1631 (1983).
[4]R. Shimizu and Z. J. Ding, "Monte Carlo modelling of electron-solid interactions," Rep. Prog. Phys. **55**, 487 (1992).
[5]C. S. Joy, *Monte Carlo Modeling for Electron Microscopy and Microanalysis* (Oxford University Press, 1995).
[6]Z. J. Ding and R. Shimizu, "A Monte Carlo modeling of electron interaction with solids including cascade secondary electron production," Scanning **18**, 92 (1996).
[7]M. Dapor, *Transport of Energetic Electrons in Solids: Computer Simulation with Applications to Materials Analysis and Characterization* (Springer, 2016).
[8]M. Dapor, *Electron Beam Interactions with Solids: Application of the Monte Carlo Method to Electron Scattering Problems* (Springer, 2003).
[9]Y. G. Li, S. F. Mao, and Z. J. Ding, "Monte Carlo simulation of SEm and SAM images," in *Applications of Monte Carlo Method in Science and Engineering*, edited by S. Mark, and S. Mordechai (IntechOpen, 2011).
[10]Z. J. Ding, C. Li, B. Da, and J. Liu, "Charging effect induced by electron beam irradiation: A review," Sci. Technol. Adv. Mater. **22**, 932 (2021).

[11]L. Reimer, *Scanning Electron Microscopy: Physics of Image Formation and Microanalysis* (Springer, 1985).
[12]C. G. Frase, D. Gnieser, and H. Bosse, "Model-Based SEM for dimensional metrology tasks in semiconductor and mask industry," J. Phys. D: Appl. Phys. **42**, 183001 (2009).
[13]C. G. Frase, E. Buhr, and K. Dirscherl, "CD characterization of nanostructures in SEM metrology," Meas. Sci. Technol. **18**, 510 (2007).
[14]S. Babin, K. Bay, and J. J. Hwu, "Application of analytic scanning electron microscopy to critical dimensions metrology at nanometer scale," J. Vac. Sci. Technol. B, Nanotechnol. Microelectron. Mater., Process., Meas., Phenom. **28**, C6H1 (2010).
[15]J. Matsumoto, Y. Ogiso, M. Sekine, T. Iwai, and J. Whittey, "A New algorithm for SEM critical dimension measurements for differentiating between lines and spaces in dense line/space patterns without tone dependence," Proc.: SPIE. **6349**, 634941 (2006).
[16]K. Ueda, S. Koshihara, T. Mizuno, and A. Miura, "The study of high-sensitivity metrology method by using CD-SEM," Proc. SPIE **7971**, 613 (2011).
[17]J. S. Villarrubia, A. E. Vladar, J. R. Lowney, M. T. Postek-Jr, R. A. Allen, M. W. Cresswell, and R. N. Ghoshtagore, "Linewidth measurement intercomparison on a besoi sample," Proc. SPIE **3998**, 84 (2000).
[18]C. Shishido, Y. Takagi, M. Tanaka, O. Komuro, H. Morokuma, and K. Sasada, "Characterizing cross-sectional profile variations by using multiple parameters extracted from Top-down SEM images," Proc. SPIE **4689**, 653 (2002).
[19]T. Onozuka, Y. Ojima, J. Meessen, and B. Rijpers, "Estimation of pattern shape based on CD-SEM image by using MPPC method," Proc. SPIE **6152**, 484 (2006).
[20]J. S. Villarrubia, A. E. Vladár, and M. T. Postek, "A simulation study of repeatability and bias in the CD-SEM," Proc. SPIE **5038**, 138 (2003).
[21]C. G. Frase, W. Häßler-Grohne, G. Dai, H. Bosse, Y. A. Novikov, and A. V. Rakov, "SEM linewidth measurements of anisotropically etched silicon structures smaller than 0.1μm," Meas. Sci. Technol. **18**, 439 (2007).
[22]S. Babin, S. Borisov, A. Ivanchikov, and I. Ruzavin, "CHARIOT: Software tool for modeling SEM signal and e-beam lithography," Phys. Procedia **1**, 305 (2008).
[23]M. Ciappa, A. Koschik, M. Dapor, and W. Fichtner, "Modeling secondary electron images for linewidth measurement by critical dimension scanning electron microscopy," Microelectron. Reliab. **50**, 1407 (2010).
[24]B. Bunday, A. Cepler, A. Cordes, and A. Arceo, "CD-SEM metrology for Sub-10 nm width features," Proc. SPIE **9050**, 238 (2014).
[25]Y. A. Novikov, Y. V. Ozerin, A. V. Rokov, and P. A. Todua, "Method for linear measurements in the nanometre range," Meas. Sci. Technol. **18**, 367 (2007).
[26]C. G. Frase and W. Häßler-Grohne, "Use of Monte Carlo models in the development and validation of CD operators," Surf. Interface Anal. **37**, 942 (2005).
[27]M. Tanaka, C. Shishido, Y. Takagi, H. Morokuma, O. Kumuro, and H. Mori, "Cross-sectional gate feature identification using top-down SEM images," Proc. SPIE **5038**, 5038 (2003).
[28]M. P. Davidson and A. E. Vladar, "Inverse scattering approach to SEM linewidth measurements," Proc. SPIE **3677**, 640 (1999).
[29]J. S. Villarrubia, A. E. Vladar, J. R. Lowney, and M. T. Postek, "Edge determination for polycrystalline silicon lines on gate oxide," Proc. SPIE **4344**, 147 (2001).
[30]J. S. Villarrubia, A. E. Vladar, and M. T. Postek, "Simulation study of repeatability and bias in the critical dimension scanning electron microscope," J. Micro/Nanolithogr., MEMS, MOEMS **4**, 033002 (2005).
[31]L. V. Kessel and C. W. Hagen, "Nebula: Monte Carlo simulator of electron-matter interaction," SoftwareX **12**, 100605 (2020).
[32]J. S. Villarrubia, A. E. Valdar, B. D. Bunday, and M. Bishop, "Dimensional metrology of resist lines using a SEM model-based library approach," Proc. SPIE **5375**, 199 (2004).
[33]D. V. Gorelikov, J. Remillard, N. T. Sullivan, and M. Davidson, "Model-based CD-SEM metrology at low and ultralow landing energies: Implementation and results for advanced IC manufacturing," Surf. Interface Anal. **37**, 959 (2005).
[34]J. S. Villarrubia, A. E. Vladár, and M. T. Postek, "Scanning electron microscope dimensional metrology using a model-based library," Surf. Interface Anal. **37**, 951 (2005).
[35]J. S. Villarrubia, A. E. Vladár, B. Ming, R. J. Kline, D. F. Sunday, J. S. Chawla, and S. List, "Scanning electron microscope measurement of width and shape of 10 nm patterned lines using a JMONSEL-modeled library," Ultramicroscopy **154**, 15 (2015).
[36]Y. B. Zou, M. S. S. Khan, H. M. Li, Y. G. Li, W. Li, S. T. Gao, L. S. Liu, and Z. J. Ding, "Use of model-based library in critical dimension measurement by CD-SEM," Measurement **123**, 150 (2018).
[37]ISO 21466:2019(E), "Microbeam analysis—Scanning electron microscopy—Method for evaluating critical dimensions by CD-SEM."
[38]J. S. Villarrubia and Z. J. Ding, "Sensitivity of SEM width measurements to model assumptions," Proc. SPIE **7272**, 232 (2009).
[39]L. V. Kessel, C. W. Hagen, and P. Kruit, "Surface effects in simulations of scanning electron microscopy images," J. Micro/Nanolithogr., MEMS, MOEMS **18**, 044002 (2019).
[40]L. V. Kessel, T. Huisman, and C. W. Hagen, "Understanding the influence of three-dimensional sidewall roughness on observed line-edge roughness in scanning electron microscopy images," J. Micro/Nanolithogr., MEMS, MOEMS **19**, 034002 (2020).
[41]K. T. Arat and C. W. Hagen, "Model sensitivity analysis of Monte-Carlo based SEM simulations," Results Phys. **19**, 103545 (2020).
[42]ISO-JCGM, 101, "2008 Evaluation of measurement data-supplement 1 to the 'guide to the expression of uncertainty in measurement'—Propagation of distributions using a Monte Carlo method."
[43]P. R. G. Couto, J. C. Damasceno, S. P. D. Oliveira, and W. K. Chan, "Monte Carlo simulations applied to uncertainty in measurement," in *Theory and Applications of Monte Carlo Simulations*, edited by W. K. Chan (IntechOpen, 2013).
[44]Z. J. Ding, X. D. Tang, and R. Shimizu, "Monte Carlo study of secondary electron emission," J. Appl. Phys. **89**, 718 (2001).
[45]A. Hussain, L. Yang, S. Mao, B. Da, K. Tőkési, and Z. J. Ding, "Determination of electron backscattering coefficient of beryllium by a high-precision Monte Carlo simulation," Nucl. Mater. Energy **26**, 100862 (2021).
[46]H. M. Li and Z. J. Ding, "Monte Carlo simulation of secondary electron and backscattered electron images in scanning electron microscopy for specimen with complex geometric structure," Scanning **27**, 254 (2005).
[47]Y. T. Yue, H. M. Li, and Z. J. Ding, "Monte Carlo simulation of secondary electron and backscattered electron images for a nanoparticle-matrix system," J. Phys. D: Appl. Phys. **38**, 1966 (2005).
[48]Y. G. Li, S. F. Mao, H. M. Li, S. M. Xiao, and Z. J. Ding, "Monte Carlo simulation study of scanning electron microscopy images of rough surfaces," J. Appl. Phys. **104**, 064901 (2008).
[49]P. Zhang, H. Wang, Y. G. Li, S. F. Mao, and Z. J. Ding, "Monte Carlo simulation of secondary electron images for real sample structures in scanning electron microscopy," Scanning **34**, 145 (2012).
[50]Y. G. Li, P. Zhang, and Z. J. Ding, "Monte Carlo simulation of CD-SEM images for linewidth and critical dimension metrology," Scanning **35**, 127 (2013).
[51]M. S. S. Khan, L. H. Yang, X. Deng, S. F. Mao, Y. B. Zou, Y. G. Li, H. M. Li, and Z. J. Ding, "Critical-dimension scanning electron microscope characterization of smoothly varying wave structures with a Monte Carlo simulation," J. Phys. D: Appl. Phys. **54**, 445301 (2021).
[52]C. Geuzaine and J. F. Remacle, "Gmsh: A 3-D finite element mesh generator with built-in pre and post processing facilities," Int. J. Numer. Methods Eng. **79**, 1309 (2009).
[53]N. F. Mott, "The scattering of fast electrons by atomic nuclei," Proc. R. Soc. London, Ser. A **124**(794), 425 (1929).
[54]F. Salvat, A. Jablonski, and C. J. Powell, "ELSEPA-Dirac partial-wave calculation of elastic scattering of electrons and positrons by atoms, positive ions and molecules (new version announcement)," Comput. Phys. Commun. **261**, 107704 (2021).
[55]M. S. S. Khan, S. F. Mao, Y. B. Zou, B. Da, Y. G. Li, and Z. J. Ding, "Comprehensive theoretical quantification of electrons emission from silicon," Vacuum, **2023**, 112257.

[56]P. Nozières and D. Pines, *Theory of Quantum Liquids: Superfluid Bose Liquids* (Addison-Wesley, 1988).
[57]D. R. Penn, "Electron mean-free-path calculations using a model dielectric function," Phys. Rev. B **35**, 482 (1987).
[58]Z. H. Levine and S. G. Louie, "New model dielectric function and exchange-correlation potential for semiconductors and insulators," Phys. Rev. B **25**, 6310 (1982).
[59]B. Da, H. Shinotsuka, H. Yoshikawa, Z. J. Ding, and S. Tanuma, "Extended Mermin method for calculating the electron inelastic mean free path," Phys. Rev. Lett. **113**, 063201 (2014).
[60]E. D. Palik, *Handbook of Optical Constants of Solids* (Academic Press, 1997), Vol. 1-4.
[61]B. L. Henke, P. Lee, T. J. Tanaka, R. L. Shimabukuro, and B. K. Fujikawa, "Low-energy x-ray interaction coefficients: Photoabsorption, scattering, and reflection: E = 100–2000eV Z= 1–94," At. Data Nucl. Data Tables **27**, 1 (1982).
[62]B. L. Henke, E. M. Gullikson, and J. C. Davis, "X-ray interactions: Photoabsorption, scattering, transmission, and reflection at E = 50–30,000 eV, Z= 1-92," At. Data Nucl. Data Tables **54**, 181 (1993).
[63]L. H. Yang, K. Tőkési, J. Tóth, B. Da, and Z. J. Ding, "Revision of optical property of silicon by a reverse Monte Carlo analysis of reflection electron energy loss spectroscopy spectra," J. Phys. Conf. Ser. **1412**, 202026 (2020).
[64]L. H. Yang, J. M. Gong, A. Sulyok, M. Menyhárd, G. Sáfrán, K. Tőkési, B. Da and Z, and J. Ding, "Optical properties of amorphous carbon determined by reflection electron energy loss spectroscopy spectra," Phys. Chem. Chem. Phys. **23**, 25335 (2021).
[65]C. Cohen-Tannoudji, B. Diu, and F. Laloe, *Quantum Mechanics* (Wiely, 1977).
[66]Z. J. Ding, H. M. Li, X. D. Tang, and R. Shimizu, "Monte Carlo simulation of absolute secondary electron yield of Cu," Appl. Phys. A: Mater. Sci. Process. **78**, 585 (2004).
[67]Q. Gibaru, C. Inguimbert, P. Caron, M. Raine, D. Lambert, and J. Puech, "Geant-4 physics processes for microdosimetry and secondary electron emission simulation: Extension of microelec to very low energies and 11 materials (C, Al, Si, Ti, Ni, Cu, Ge, Ag, W, Kapton and SiO_2)," Nucl. Instrum. Methods Phys. Res., Sect. B **487**, 66 (2021).
[68]E. M. Conwell, "Properties of silicon and germanium," Proc. SPIE **40**, 1327 (1952).
[69]J. Van Laar and J. J. Scheer, "Photoemission of semiconductors," Philips Tech. Rev. **29**, 54 (1968); available at https://www.pearl-hifi.com/06_Lit_Archive/02_PEARL_Arch/Vol_16/Sec_53/Philips_Tech_Review_1936_thru_1986/PTechReview-29-1968-054.pdf.
[70]L. Esaki, "Electrical resistivity and thermionic emission of silicon," J. Phys. Soc. Jpn. **8**, 347 (1953).
[71]W. E. Meyerhof, "Contact potential difference in silicon crystal rectifiers," Phys.Rev. **71**, 727 (1947).
[72]S. M. Fainshtein, "A cascade electron multiplier for photometric purposes," Zavod. Lab. **14**, 64 (1948).
[73]A. H. Smith, "Temperature dependence of the work function of semiconductors," Phys. Rev. **75**, 953 (1949).
[74]A. Braun and G. Busch, "Measurement of the electron emission from carbon, silicon and silicon carbide," Helv. Phys. Acta **20**, 33 (1947).
[75]H. B. Michaelson, "The work function of the elements and Its periodicity," J. Appl. Phys. **48**, 4729 (1977).
[76]B. M. Tsarev, *Contact Potential Difference* (GITTL, Moscow, 1955).
[77]S. S. Batsanov, "The concept of electronegativity.: Conclusions and prospects," Russ. Chem. Rev. **37**, 332 (1968).
[78]F. G. Allen, "Field emission from silicon and germanium; field desorption and surface migration," J. Phys. Chem. Solids **19**, 87 (1961).
[79]F. G. Allen and G. W. Gobeli, "Comparison of the photoelectric properties of cleaved, heated, and sputtered silicon surfaces," J. Appl. Phys. **35**, 597 (1964).
[80]C. Blondel, C. Delsart, and F. Goldfarb, "Electron spectrometry at the μeV level and the electron affinities of Si and F," J. Phys. B: At., Mol. Opt. Phys. **34**, 2757 (2001).
[81]F. Davi, V. Paratte, J. Antognini, J. Dréon, J. Hurni, J. Thomet, R. Rubinger, E. Bortoni, C. Ballif, and M. M. Boccard, "Effects of work function and electron affinity on the performance of carrier-selective contacts in silicon solar cells using ZNSN," IEEE J. Photovolt. **11**, 6 (2021).
[82]ISO-JCGM, 100, "2008 Evaluation of measurement data-guide to the expression of uncertainty in measurement."
[83]H. Zhang, J. Tang, J. Yuan, Y. Yamauchi, T. T. Suzuki, N. Shinya, K. Nakajima, and L. C. Qin, "An ultrabright and monochromatic electron point source made of a Lab6 nanowire," Nat. Nanotechnol. **11**, 273 (2016).
[84]A. Hussain, L. H. Yang, Y. B. Zou, B. Da, S. F. Mao, H. M. Li, and Z. J. Ding, "Monte Carlo simulation study of secondary electron emission from semiconductor materials," J. Appl. Phys. **128**, 015305 (2020).